Influence of absorption-edge properties on subpicosecond intrinsic laser-damage threshold at 1053 nm in hafnia and silica monolayers

M Chorel, S Papernov, A A Kozlov, B N Hoffman, J B Oliver, S G Demos, T Lanternier, É Lavastre, L Lamaignère, N Roquin, et al.

Research Article | Vol. 27, No. 12 | 10 Jun 2019 | OPTICS EXPRESS 16922
Optics EXPRESS

Influence of absorption-edge properties on subpicosecond intrinsic laser-damage threshold at 1053 nm in hafnia and silica monolayers

M. Chorel,[1,*] S. Papernov,[2] A. A. Kozlov,[2] B. N. Hoffman,[2] J. B. Oliver,[2] S. G. Demos,[2] T. Lanternier,[1] É. Lavastre,[1] L. Lamaignère,[1] N. Roquin,[1] B. Bousquet,[3] N. Bonod,[4] and J. Néauport[1]

[1]*Commissariat à l'Energie Atomique et aux Energies Alternatives, Centre d'Etudes Scientifiques et Techniques d'Aquitaine (CEA CESTA), F-33116 Le Barp, France*
[2]*Laboratory for Laser Energetics, University of Rochester, 250 E. River Road, Rochester, NY 14623-1299, USA*
[3]*CELIA, Université de Bordeaux UMR5107, 33400 Talence, France*
[4]*Aix Marseille Univ, CNRS, Centrale Marseille, Institut Fresnel, 13013 Marseille, France*
**marine.chorel@cea.fr*

Abstract: Owing to their relatively high resistance to laser-induced damage, hafnia and silica are commonly used in multilayered optical coatings in high-power laser facilities as high- and low-refractive-index materials, respectively. Here, we quantify the laser-induced–damage threshold (LIDT) at 1053 nm in the short-pulse regime of hafnia and silica monolayers deposited by different fabrication methods, including electron-beam evaporation, plasma ion-assisted deposition and ion-assisted deposition. The results demonstrate that nominally identical coatings fabricated by different deposition techniques and/or vendors can exhibit significantly different damage thresholds. A correlation of the LIDT performance of each material with its corresponding absorption edge is investigated. Our analysis indicates a weak correlation between intrinsic LIDT and the optical gap of each material (Tauc gap) but a much better correlation when considering the spectral characteristics in the Urbach tail spectral range. Spectrophotometry and photothermal absorption were used to provide evidence of the correlation between the strength of the red-shifted absorption tail and reduced LIDT at 1053 nm.

1. Introduction

The past decades have seen the construction of petawatt-class laser facilities [1] such as FIREX [2], OMEGA EP [3], and Petal [4,5]. The overall power output in these systems is currently limited by the laser-induced-damage threshold (LIDT) of the optical components located after the compression stage. Among the different optical elements, multilayer dielectric (MLD) mirrors are of vital importance for transporting the laser beam to the target chamber.

Improving our understanding of the physical processes governing laser-induced damage in thin-film coatings is necessary to design and fabricate optical components that provide higher damage resistance. Recent work has shown that damage with ultrashort pulses (shorter than about 2.5 ps) in hafnia/silica MLD coatings is initiated by electric-field–induced volume breakdown [6]. To understand the origin of laser damage in MLD-coated optics in the short-pulse regime, one needs to consider the difference between the damage threshold of the tested optic and the damage threshold of the constituent materials involved. This is because the intensity of the electric field within each layer varies significantly, depending on the design of

#361219 https://doi.org/10.1364/OE.27.016922
Journal © 2019 Received 27 Feb 2019; revised 26 Apr 2019; accepted 26 Apr 2019; published 3 Jun 2019

Optics EXPRESS

the multilayer, giving rise to a distribution of enhanced electric-field intensity within each layer structure [7–9]. As a result, the material within each individual layer is exposed to a depth-dependent variation of the electric field. Damage is initiated when the electric-field intensity (localized laser fluence) reaches a value above the threshold value of one of the materials (the damage threshold of the material, also referred to as "intrinsic" damage threshold). As a result, damage can be initiated at different depths and/or layers within the same optic, depending on the irradiation parameters such as angle of incidence and polarization state of the laser beam. At damage-threshold conditions, the material volume exposed to a narrow range of peak electric-field intensities (that can support plasma formation) is superheated. The generated pressure in this volume must also be sufficient to support shear fracture and detachment of the overlying layer [6]. Therefore, to a first approximation, the damage threshold of the tested optic ($LIDT_{meas}$) is determined by the damage threshold of each material within the coating ($LIDT_{int}$) normalized by the peak electric-field enhancement (EFI_{max}): $LIDT_{int} = LIDT_{meas} \times EFI_{max}$.

Mero *et al.* [10] established a link between the $LIDT_{int}$ of monolayers in J/cm^2 with the band-gap energy E_g of the material in eV. More recently, Hervy *et al.* [11] reported similar observations and established an empirical expression involving a linear dependence between the band-gap energy and the intrinsic LIDT: $LIDT_{int} = 0.6 \times E_g – 1.45$. This formulation clearly establishes the usage of high electronic band-gap materials to achieve maximum intrinsic LIDT. However, determining the intrinsic LIDT remains a challenge, and the linear dependence with the band-gap energy has been established within a single deposition technique. Gallais *et al*. [12] showed a large variation of the intrinsic LIDT when the same material is deposited with different techniques. The range of $LIDT_{int}$ is particularly large for hafnia. For practical use, it is imperative to develop an accurate relationship between the material's electronic structure and its corresponding optical properties with its laser-damage resistance.

As mentioned above, damage initiation with short pulses is associated with the formation of plasma that facilitates, via a complex energy deposition process, superheating of the affected volume. Assuming a crystalline material, the buildup of the electron density in the conduction band commences with multiphoton excitation between the ground state and conduction band. The layers in MLD coatings are generally amorphous, however, so their structure can vary based on the deposition method. Consequently, the optical absorption can be characterized by an optical gap that most often is analyzed using two methods. At photon energies above the optical gap, the absorption (α) behaves according to the Tauc formula, i.e., $\alpha\hbar\omega \propto (\hbar\omega - E_T)^2$, where E_T is known as the *Tauc gap*. Below the optical gap, the absorption is described by the Urbach tail [13] that arises from localized states in the band gap. In addition, defect states can further extend the absorption edge toward lower energies. As a result, transitions from the ground state to the conduction band are not limited to intraband transitions but include additional pathways through intermediate states at the Urbach tail and defects. It has been previously discussed that red-shifting of the Urbach tail can lead to a reduced damage threshold in silica [14]. The role of defects in decreasing the damage threshold has also been documented in various materials including hafnia monolayers [15].

The focus of the present work is to investigate the relationship of LIDT (intrinsic LIDT) of silica and hafnia layers obtained via different fabrication processes (different deposition methods and different vendors) to characteristic optical signatures of the material. Hafnia and silica are chosen since they are ubiquitous in MLD components used in high-power laser systems. By calculating the electric-field distribution inside the different samples, we estimate the $LIDT_{int}$ for the different samples using the measured damage threshold of each sample. The damage thresholds are investigated as a function of the estimated optical gap (Tauc gap) of each material and further evaluated as a function of the red-shifted absorption tails using

Optics EXPRESS

photothermal absorption and spectroscopic analysis in the UV spectral region. In the following section, we will present the set of materials and characterization methods employed in this study. The results and discussion will be in the third section. These results are accompanied by estimations of uncertainties carried out on each characterization method in accordance with [16] and [17]. The determination of uncertainties is detailed in the methods section.

2. Materials and methods

2.1. Description of samples

Silica and hafnia monolayers deposited by various research groups and commercial vendors using different deposition methods were used in this work. These deposition methods include plasma ion-assisted deposition (PIAD), electron-beam evaporation with and without ion assistance [ion-assisted e-beam deposition (IAD), and e-beam], IAD samples were acquired from two different vendors.

The different characterization techniques involved in this work required specific types of substrates. The refractive index has been determined with ellipsometry, requiring silicon wafers with a large refractive-index contrast with the layer. The LIDT determination requires high LIDT substrates; for that purpose we preferred fused silica and BK7 substrates fabricated with the same polishing and cleaning requirements as full-size laser optics. Spectrophotometry measurements require transparent substrates and have been performed on samples deposited on fused-silica substrates. The photothermal heterodyne imaging measurements were performed on the same samples used for the LIDT characterization. For each fabrication process, layers were deposited simultaneously on all of the different substrates in order to obtain the same nominal layer properties (thickness and density). The different coating techniques and substrates are detailed in Table 1 for hafnia layers and Table 2 for silica layers presented in 3.1.

2.2. Determination of the refractive index and thickness

To determine the optical thickness and electric-field distribution within each layer, the refractive index and thickness of the layers must be accurately determined. Such data are provided by the vendors. It is assumed that the layer deposition is controlled with less than 5% error on the thickness and refractive index. However these uncertainties are too high for our study. In order to reduce these uncertainties and thereby uncertainties on the EFI_{max} calculation, the choice was made to independently remeasure these values. First, the refractive index and physical thickness of the monolayers deposited on silicon wafers were determined by ellipsometry. In this technique, the ellipsometric angles Ψ and Δ of the reflected wave (with a 70° angle of incidence) are determined for multiple wavelengths, where $\tan(\Psi)$ is the ratio of the *p*- and *s*-polarized amplitude reflectance and Δ is the reflected phase shift. With OptiChar it is possible to fit the ellipsometry and spectrophotometry measurements simultaneously [18]. Accordingly, in addition to the ellipsometric measurements, reflection spectra of the monolayers deposited on the silicon wafer were acquired with a spectrophotometer (Perkin Elmer lambda 950 Flex System) at 8° and 45° for both polarizations. Reflection and ellipsometric angle measurements were fit to retrieve the refractive index and the physical thickness.

Uncertainties on the determination of the layer thickness and refractive index are due to experimental errors (offset, noise level). In order to evaluate their impact, we use a numerical method. The reflection spectra $R(\lambda)$ at 8° and 45° and ellipsometric angles $\Psi(\lambda)$ and $\Delta(\lambda)$ at 70° of a theoretical monolayer of either hafnia or silica on a silicon wafer are first calculated. A white noise mimicking an experimental noise monitored by the spectrophotometer or ellipsometer is subsequently added to the spectra. The intensity of this noise is set to be a majoring value of the noise observed on our experimental data. These spectra are then fit with

Optics EXPRESS

the Optichar software with respect to the refractive index and thickness of the monolayer. The uncertainties u_n and u_h are obtained by calculating the maximal difference between the fit and the initial values of n and h. The choice of the refractive-index dispersion model has more impact on the error for the refractive index and thickness than the level of noise. Still, with this method and regardless of the dispersion model, the uncertainty is reduced to $\pm 2.5 \times 10^{-2}$ for the refractive index and to ± 5 nm for the thickness. The refractive index and thickness of each layer are determined simultaneously by fitting measurements, and, therefore, their uncertainties (u_n and u_h, respectively) are correlated.

In addition, reflection and transmission spectra of monolayers deposited on fused-silica windows were acquired at 8° and 45° and then fit using OptiChar to calculate the refractive-index dispersion and physical thickness. This second technique was used to verify that layers deposited on both substrates were identical.

2.3. Intrinsic LIDT determination

2.3.1. EFI calculation

Values of the refractive index and thickness measured in the previous section are now used to calculate the electric-field intensity distribution within each monolayer. The electric-field intensity was calculated numerically using two independent approaches, the OptiLayer software, and a MATLAB code that incorporates the matrix formalism described in [19]. The sample is modeled as a monolayer deposited on a semi-infinite substrate (either fused silica or BK7 depending on the sample) and the superstrate with a refractive index of 1. The sample is illuminated at normal incidence from the superstrate with a plane wave linearly polarized at the wavelength λ = 1053 nm. The distribution of the square of the time-averaged electric field $|E|^2$ is calculated and normalized by the incident electric field $|E_0|^2$. The maximum enhancement of the electric-field intensity in the layer, $|E|^2 / |E_0|^2$ denoted by $\mathrm{EFI_{max}}$, is estimated and reported in Tables 1 and 2.

The laser used in the damage test setup (discussed next in more detail) was operating with a 2.8 nm bandwidth centered on λ = 1053 nm. The electric-field distribution depends on multiple variables (laser wavelength λ and bandwidth, angle of incidence θ, polarization, refractive index n, and thickness h of the layers); consequently, the evaluation of the uncertainty on the $\mathrm{EFI_{max}}$ must include all above sources of uncertainty. The influence of the spectral bandwidth on the $\mathrm{EFI_{max}}$ can be safely neglected. To evaluate the standard uncertainty on the $\mathrm{EFI_{max}}$, we first calculate the maximum of the electric-field intensity (Fig. 1) inside a layer of refractive index n_L deposited on a substrate of refractive index n_S for every angle of incidence (y axis) and for both polarizations when increasing the layer's physical thickness from 0 to 1000 nm (x axis). We applied this technique to the three kinds of samples: hafnia layer on a fused-silica or BK7 substrate [Fig. 1(a)], silica layer on a fused-silica substrate [Fig. 1(b)], and silica layer on BK7 substrates [Fig. 1(c)]. Results displayed in Fig. 1 show that the $\mathrm{EFI_{max}}$ depends mostly on the refractive-index contrast between the layer and the substrate. For hafnia layers, the refractive-index contrast is important while for the silica layers, it is weak, so the choice of substrate significantly affects the uncertainty evaluation.

As an example, we detail this parametric approach on only the first kind of sample: a hafnia layer (n_L = 1.95) on a fused-silica substrate (n_S = 1.45). According to [16], the uncertainty of the $\mathrm{EFI_{max}}$, $u_{\mathrm{EFI_{max}}}$, can be calculated as a combined standard uncertainty:

$$u_{\mathrm{EFI_{max}}}^2 = \left[\frac{\partial(\mathrm{EFI_{max}})}{\partial h}\right]^2 \times u_h^2 + \left[\frac{\partial(\mathrm{EFI_{max}})}{\partial n}\right]^2 \times u_n^2 + \left[\frac{\partial(\mathrm{EFI_{max}})}{\partial \theta}\right]^2 \times u_\theta^2 + 2\frac{\partial(\mathrm{EFI_{max}})}{\partial h}\frac{\partial(\mathrm{EFI_{max}})}{\partial n} \times u_h u_n \times r(n,h), \quad (1)$$

Optics EXPRESS

where $r(n,h)$ is the correlation factor between the refractive index and the thickness.

To apply this formula, the derivative of the electric field, shown in Fig. 2, is considered for the three remaining sources of uncertainty: physical thickness [Fig. 2(a)] and refractive index [Fig. 2(b)] of the layer and finally the angle of incidence [Fig. 2(c)].

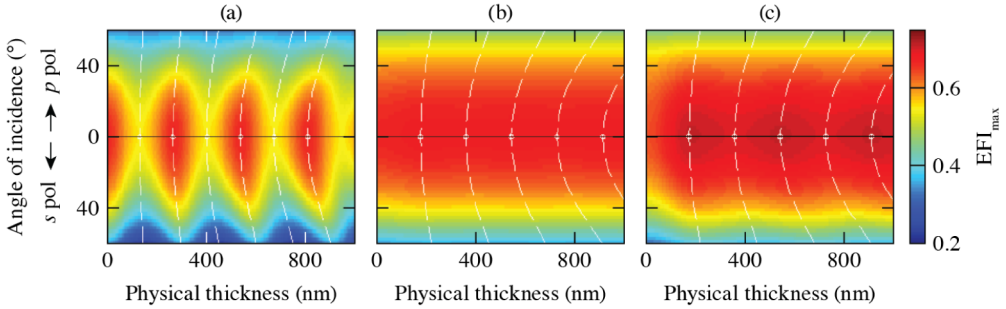

Fig. 1. EFI_{max} (color scale) as functions of the layer thickness (x axis) and angle of incidence (y axis) for p (positive y) and s (negative y) polarization: (a) hafnia layer (n_L = 1.95) on a fused-silica substrate (n_S = 1.45), (b) silica layer (n_L = 1.44) on a fused-silica substrate (n_S = 1.45), and (c) silica layer (n_L = 1.44) on a BK7 substrate (n_S = 1.50). Dashed white lines indicate the multiple of $\lambda/4$ optical thicknesses.

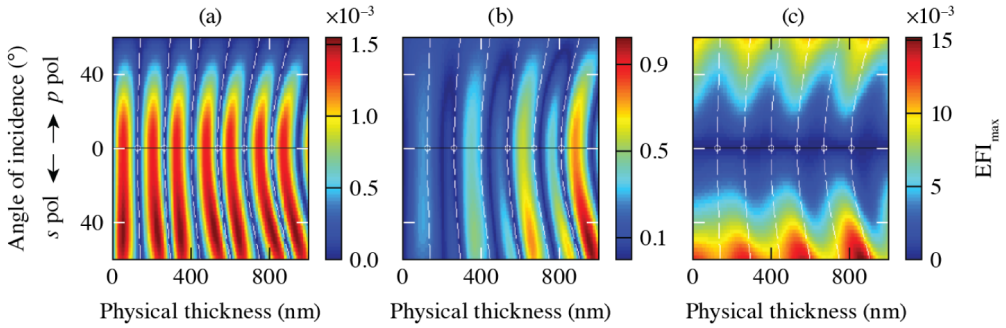

Fig. 2. Derivative of the electric-field maximum regarding (a) the thickness $[\partial(EFI_{max})/\partial h]^2$, (b) refractive index $[\partial(EFI_{max})/\partial n]^2$ of the monolayer, and (c) angle of incidence $[\partial(EFI_{max})/\partial\theta]^2$ for a hafnia layer (n_L = 1.95) on a fused-silica substrate (n_s = 1.45).

Figure 2(a) shows that it is preferable to have an optical thickness that is an integer multiple of $\lambda/4$ to minimize the sensitivity to thickness errors, which is reasonable since this corresponds to extrema in the electric field at the coating/incident media interface. Figure 2(b) indicates that the uncertainty on the EFI_{max} resulting from the refractive index error oscillates with the layer thickness (again aligned with electric-field extrema at the coating/incident media interface) and that the amplitude of oscillations increases with the thickness. Figure 2(c) highlights that carrying out the damage tests at normal incidence reduces the uncertainties coming from the angle of incidence.

The error on the angle of incidence u_θ depends on the precision of the position stage of the sample carrier of the damage setup. The standard uncertainty on the angle of incidence is coming from the position stage and is evaluated to ± 0.1°.

Errors on the thickness and on the refractive index are correlated. The extreme values of the correlation factor $r(n,h)$: (–1, 0, and 1) are considered for the calculations [16]. The final uncertainty on the EFI_{max} is defined as the worst case of the three calculations described above. Following these results, the damage tests of our entire set of samples will be performed at normal incidence. The standard uncertainties on the EFI_{max} evaluated with this approach for each sample are reported in Tables 1 and 2.

Optics EXPRESS

2.3.2. Laser-damage testing measurements

The LIDT of each sample is determined with a 1-on-1 procedure on a laser-damage setup DERIC installed at CEA CESTA [20]. DERIC uses an S-pulse Amplitude Systèmes laser source delivering a Gaussian beam at 1053 nm. The pulse duration can vary between 800 fs and 4 ps and is estimated from the autocorrelation trace measurement provided by a recurrent autocorrelator (PulseCheck APE). On the sample, the Gaussian-shaped focal spot has a 150-mm diameter at 1/*e* of its maximum intensity profile. For each pulse, the energy and the beam diameter are measured in a sampling path with, respectively, an Ophir calorimeter and a Cohu camera 4713 from Spiricon placed at an optically equivalent plane to the sample plane. The energy measured in the sampling path is used to predict the precise fluence of every shot on the sample. The uncertainties coming from the setup are caused by the calibration of the setup, which is at $u_{\mathrm{DERIC}} = \pm 5\% \times$ fluence, and the day-to-day repeatability of tests, which is estimated at $u_{\mathrm{repeat}} = \pm 2.5\% \times$ fluence.

The *in situ* damage detection is done by analyzing the variation of the scattered light from the focal spot. Damage is recorded when the scattered light increases. This *in situ* detection is used only as an indicator of the damage during the 1-on-1 procedure and not as a damage determination. The final criterion to define damage is a modification, e.g., pits or discoloration, on the sample that can be seen with a differential interferential contrast (DIC) microscope (AXIO Imager.A2, ZEISS, with 0.90 NA, 100 × objective).

Because damage in the subpicosecond regime is deterministic, there is no need to perform a statistical analysis by reproducing the measurement on several spots *per* fluence in the 1-on-1 procedure. The LIDT is defined as the mean between (1) the lowest fluence where damage is detected and (2) the highest fluence where no damage occurs. The uncertainty of the measurement u_{meas} is set to be the mean absolute deviation between these two fluences. Therefore, the uncertainty of the measurement is reduced by testing additional fluences around the damage-threshold fluence. Those tests were all performed at the minimal pulse duration of DERIC, 800 fs.

The uncertainty on the LIDT determination $u_{\mathrm{LIDT_{meas}}}$ is a combination of uncertainties resulting from the setup, the repeatability, and the measurement:

$$u_{\mathrm{LIDT_{meas}}} = \sqrt{u_{\mathrm{meas}}^2 + u_{\mathrm{DERIC}}^2 + u_{\mathrm{repeat}}^2}. \tag{2}$$

2.3.3. Estimation of the damage threshold of coating layer materials

The intrinsic LIDT value of the coating material in each sample is estimated by calculating the product between the measured LIDT of the sample and the maximum of the electric-field enhancement, $\mathrm{LIDT} \times \left|E/E_0\right|^2$, within the monolayer. We use the scaling law, $\mathrm{LIDT_{int}}$ (700 fs) = $\mathrm{LIDT_{int}}$ (τ_{exp}) × $(700/\tau_{\mathrm{exp}})^{1/3}$, established by Mero *et al.* [10] to normalize the intrinsic LIDT at the time duration of PETAL (700 fs) from the values obtained on the DERIC facility delivering 800-fs pulses.

Tables 1 and 2 provide the intrinsic LIDT ($\mathrm{LIDT_{int}}$) obtained for the different samples. The intrinsic LIDT of each material depends on the $\mathrm{EFI_{max}}$ and the measured LIDT of the corresponding sample, which means its uncertainty can be described as:

$$u_{\mathrm{LIDT_{int}}} = \sqrt{\left(\mathrm{LIDT_{meas}} \times u_{\mathrm{EFI_{max}}}\right)^2 + \left(\mathrm{EFI_{max}} \times u_{\mathrm{LIDT_{meas}}}\right)^2}. \tag{3}$$

The expanded *or overall* uncertainty of $U_{\mathrm{LIDT_{int}}} = k \times u_{\mathrm{LIDT_{int}}}$ is calculated by multiplying with the coverage factor k taken here to be equal to 2 [16,17].

Optics EXPRESS

2.4. Optical gap determination using Tauc method

It is commonly accepted that the intrinsic LIDT has a linear relationship with the band-gap energy [10–12,21]. As discussed in Sec. 1, the as-deposited material can exhibit variations in its electronic structure and defect concentration, while its optical absorption can be characterized in part by an optical gap that is estimated by the Tauc formula. Accordingly we employed the Tauc method [22] using ultraviolet ellipsometry measurements on silicon wafer witnesses to estimate the optical gap energy for each material. Results are reported in Tables 1 and 2. In the Tauc method, the value of $\sqrt{\alpha h\nu}$ is plotted against the photon energy $h\nu$, where α is the absorption. A portion of this curve can be fitted linearly. The intersection of this linear fit with the x axis gives the Tauc gap energy in eV.

2.5. Absorption below the optical gap measurements

2.5.1. Spectrophotometry measurements

Laser-induced damage under subpicosecond pulse excitation results from a multiphoton absorption process [23]. The multiphoton absorption cross section is enhanced when intermediate states exist [24,25], which is considered to contribute a reduced damage threshold. We therefore investigate the absorption of the monolayers in the UV spectrum in order to probe the absorption characteristics of each material at energies below the optical gap (Tauc energy) as a function of the deposition technique. For that purpose, the transmission and reflection spectra of the samples are measured at near-normal incidence (8° incidence) in the range of 200 to 700 nm. The losses (arising from absorption and scattering) are then calculated from these transmission and reflection spectra $L = 1–T–R$. In the spectral region where the reduction of the transmission caused by absorption is higher than about 10%, the optical scattering can be safely neglected; therefore, we will consider losses caused only by absorption, $A = L$. On the other hand, the uncertainty on the estimated absorption coefficient increases when the absorption is very low; this is the case for silica at longer wavelengths. From these losses, the absorption coefficient is calculated as $\alpha = –(1/h)\ \ln(L)$ with h the physical thickness of the layer and L the losses previously described. These absorption coefficient spectra are plotted in Fig. 4(a) for hafnia layers and Fig. 4(b) for silica layers in sub-section 3.3.1.

2.5.2. Photothermal heterodyne imaging

To further explore the above concept, photothermal absorption measurements in the UV at 355 nm were performed using a photothermal heterodyne imaging (PHI) system. This technique described in [15] and [26] is based on a pump–probe approach. The 355-nm pump beam modulated at 410 Hz and the cw 633-nm probe beam are collinearly combined on the entrance aperture of a high-numerical-aperture objective and focused onto the sample in an overlapping submicrometer spot. The transmitted probe beam is analyzed by a photodiode coupled with a lock-in amplifier where the output signal is proportional to absorption. For every characterization, we acquired several intensity maps by raster scanning the sample over a 20 × 20-μm^2 area. Those maps were uniform, and an average value of every map for each sample was calculated. The photothermal absorption was normalized by the physical thickness of the layer. The results are displayed in Fig. 5 in sub-section 3.3.2. The uncertainty on the PHI signal is set at the noise level of this signal.

3. Results and discussion

3.1. Materials, index, thickness, intrinsic LIDT, and optical gap

The results from the sample set used in this study, summarized in Tables 1 and 2, evidence the important variation of the intrinsic LIDT with the deposition/fabrication process for both silica and hafnia. For hafnia, while low $LIDT_{int}$ values are reported with PIAD samples (0.66

Optics EXPRESS

J/cm^2), much larger values are measured with IAD layers deposited by vendor 1 (1.83 J/cm^2) and even larger for the IAD 2 layer from vendor 2 (2.70 J/cm^2). For silica, PIAD samples also exhibit the weakest intrinsic LIDT. E-beam and IAD layers by vendor 2 are seen to offer higher intrinsic LIDTs than those deposited with IAD by vendor 1. The best samples for silica are obtained here with non-assisted e-beam evaporation ($LIDT_{int}$ = 4.27 J/cm^2).

Table 1. Measured parameters for the hafnia samples.

Deposition technique	Substrate	Refractive index at 1053 nm	Physical thickness of layer (nm)	EFI_{max} (%)	LIDT measured at 800 fs (J/cm^2)	$LIDT_{int}$ 700 fs (J/cm^2)	Optical (Tauc) gap (eV)
PIAD 1	FS/Si wafer	2.01	142.7	53.9 ± 1.66	1.28 ± 0.08	0.66 ± 0.11	5.5 ± 0.025
PIAD 2	FS/Si wafer	1.96	527.2	66.4 ± 0.88	1.22 ± 0.08 (870fs)	0.75 ± 0.11	5.75 ± 0.025
IAD, vendor 1	FS/Si wafer	2.03	138.4	53.4 ± 1.58	3.59 ± 0.28	1.83 ± 0.26	5.5 ± 0.03
IAD, vendor 2	FS/Si wafer	1.95	149.5	55.56 ± 1.65	5.08 ± 0.28	2.70 ± 0.36	6 ± 0.035
	BK7/Si wafer			54.14 ± 1.54	5.11* ± 0.29	2.65 ± 0.36	
e-beam	FS/Si wafer	1.86	522.2	61.25 ± 2.16	3.37 ± 0.20	1.97 ± 0.29	5.6 ± 0.05

*LIDT measured on the layer deposited on BK7 substrate. FS: fused silica.

Table 2. Measured parameters for the silica samples.

Deposition technique	Substrate	Refractive index at 1053 nm	Physical thickness of layer (nm)	EFI_{max} (%)	LIDT measured at 800 fs (J/cm^2)	$LIDT_{int}$ 700 fs (J/cm^2)	Optical (Tauc) gap (eV)
PIAD 1	FS/Si wafer	1.46	204.0	66.5 ± 0.63	2.19 ± 0.16 (870 fs)	1.36 ± 0.21	7.6 ± 0.04
PIAD 2	FS/Si wafer	1.46	972.9	66.6 ± 0.43	2.36 ± 0.14	1.46 ± 0.18	7.4 ± 0.035
IAD, vendor 1	FS/BK7/ Si wafer	1.42	321.8	68.95 ± 3.81	4.6* ± 0.33	3.16 ± 0.53	7.2 ± 0.04
IAD, vendor 2	FS/Si wafer	1.45	202.8	67 ± 4.07	5.06 ± 0.30	3.25 ± 0.58	6.75 ± 0.55
e-beam	FS/Si wafer	1.44	797.9	67.9 ± 3.63	6.57 ± 0.37	4.27 ± 0.69	6.85 ± 0.55

*LIDT measured on the layer deposited on BK7 substrate. FS: fused silica.

3.2. Correlation of $LIDT_{int}$ to the optical gap (Tauc energy)

Results reported in Tables 1 and 2 show a weak dependence of the spectroscopically determined Tauc energy on the fabrication process for both silica and hafnia layers. Figure 3 shows $LIDT_{int}$ as a function of the optical gap energy. These results suggest that for each coating process, the intrinsic LIDT increases as a function of the optical gap energy, a trend that has also been observed in [10–12]. The results displayed in Fig. 3 further suggest that the influence of the deposition process on the optical gap energy is different for the two materials. The IAD layers by vendor 2 (red) exhibit the highest and lowest estimated optical gap energy for hafnia and silica, respectively. We observe a different trend for the layers coated by IAD by vendor 1 (orange) for which the hafnia optical gap energy is the lowest for hafnia but the silica optical gap is in the range of other silica optical gaps. The results shown in Fig. 3 also demonstrate that although the fabrication process has a large influence on the intrinsic LIDT, it only marginally affects the estimated optical gap energy. Therefore, it is not possible at this stage to establish a general law predicting the intrinsic LIDT by measuring the optical gap energy alone.

Optics EXPRESS

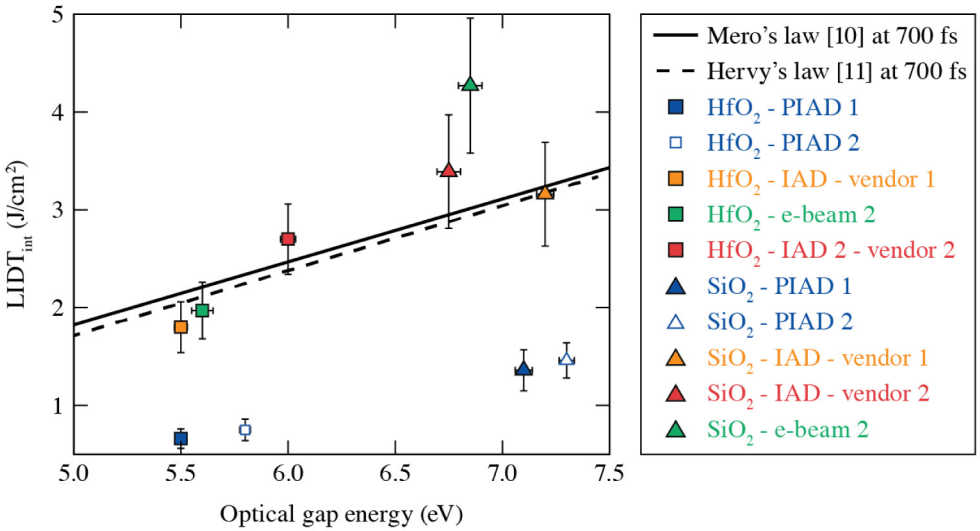

Fig. 3. Intrinsic LIDT as a function of the optical gap energy for hafnia (squares) and silica (triangles) samples deposited by PIAD (blue), IAD by vendor 1 (orange) and by vendor 2 (red), e-beam (green) compared to prediction rules taken in [10,11].

3.3. Correlation of LIDT$_{int}$ to absorption below the optical gap

3.3.1. Spectrophotometry measurements

The results displayed in Fig. 4 include the spectral region covering the red-shifted tail of the absorption edge of each material. An increase in absorption is observed for some materials starting from 351 nm. Defect states in this wavelength range can be populated via a three-photon absorption process. Additional absorption from this state will accordingly reduce the order of the multiphoton process required to support transition of electrons to the conduction band. All materials exhibit increased absorption at 210 nm, which corresponds to a five-photon absorption energy level. Based on Fermi's golden rule, the transition probability between two states depends on the strength of the perturbation matrix element ($\langle f|H|i\rangle$, where $|f\rangle$ and $|i\rangle$ are the final and initial states, respectively, and H is the time-dependent perturbation between the final and initial states) and the density of final states $\rho(E_f)$. This is manifested in the strength of the absorption at the corresponding energy levels (E_f). These fundamental concepts suggest that increased absorption in the 200- to 350-nm spectral range could be associated with decreased damage thresholds since these intermediate states increase the probability for transition of ground-state electrons to the conduction band; therefore the damage-threshold electron density can be reached at a lower laser fluence/intensity.

The results shown in Fig. 4 for hafnia layers indicate that the highest LIDT$_{int}$ samples exhibit lowest absorption in the three- to five-photon absorption spectral range (≈200 to 350 nm), while the lowest LIDT samples exhibit the highest absorption. The silica layers also exhibit the same general behavior. This trend is quantified in the insets shown in Figs. 4(a) and 4(b), which represent the absorption coefficient of hafnia monolayers at 351 nm and silica monolayers at 266 nm as a function of their intrinsic LIDT, respectively. The choice of the wavelength to represent the dependence of the LIDT as a function of the absorption coefficient is based on using a (an exemplary) threshold absorption coefficient value of the order of 10^3 cm^{-1}. These results suggest the presence of a correlation between the absorption at energies below the optical gap and the intrinsic LIDT at 1053-nm, 800-fs laser pulses. This suggests that there may be a way to model the LIDT$_{int}$ performance based on the direct measurement of the absorption spectra in the spectral region below the optical gap. Additional work is required to develop such a method that is outside the scope of the present work.

Optics EXPRESS

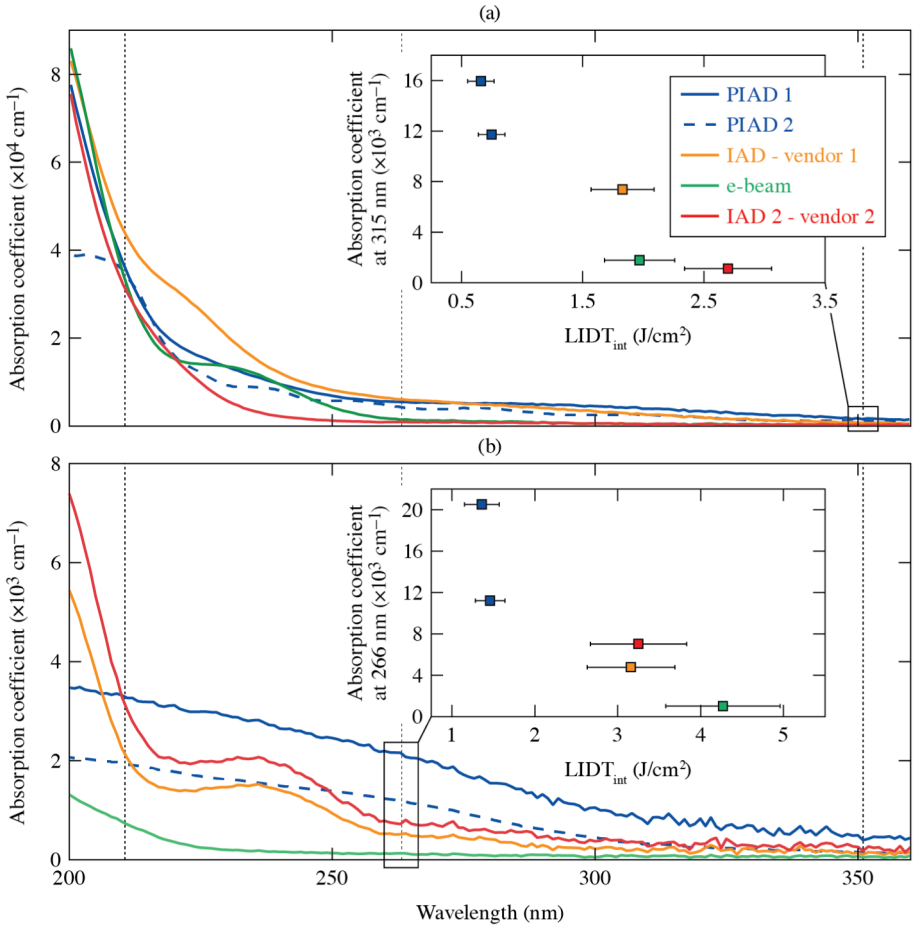

Fig. 4. Absorption coefficient at energies below the optical gap of hafnia (a) and silica (b) monolayers deposited on fused-silica substrates. Insets show the absorption coefficient of hafnia (at 351 nm) and silica (at 266 nm) as a function of their intrinsic LIDT.

3.3.2. Photothermal absorption

The results shown in Fig. 5 indicate that the strength of the photothermal absorption in the samples depends on their deposition method. For the case of hafnia samples, the highest absorption at 355 nm is obtained for the two samples (PIAD 1 and 2) that also feature the lowest $LIDT_{int}$ at 1053 nm. On the other hand, lower absorption is observed for the IAD samples by vendor 2 that also feature the highest $LIDT_{int}$. The only divergence from this trend is for the e-beam hafnia sample, which exhibits the lowest photothermal absorption signal at 355 nm, barely above noise level, but still its $LIDT_{int}$ is lower than the IAD samples from vendor 2 that exhibit slightly higher photothermal absorption. This behavior might indicate that there are additional processes affecting the $LIDT_{int}$ that are not captured by the photothermal absorption technique when using a 355-nm pump. In fact, the absorption spectrum of the e-beam sample shown in Fig. 4(a) indicates that its absorption at wavelengths longer than 266 nm (corresponding to defect states that can be excited via three- or four-photon absorption) is very small, but it rapidly increases at shorter wavelengths to reach one of the highest values at wavelengths corresponding to states that can be excited by five-photon absorption. This observation may suggest that complementary photothermal measurements at higher laser harmonics may be required for a more accurate assessment of the $LIDT_{int}$ using the photothermal absorption method.

Optics EXPRESS

The general trend observed in the hafnia samples is also observed for the silica samples. The number of data points for silica is limited since absorption of fused silica is very low and below the detection limit of our instrumentation. Specifically, we were able to measure photothermal absorption for the PIAD samples only, which also exhibited the weakest $LIDT_{int}$ values. A correlation between photothermal absorption at 355 nm and $LIDT_{int}$ at 1053 nm seems to be observed for both hafnia and silica monolayers. This correlation could open novel routes toward a nondestructive characterization of the intrinsic LIDT.

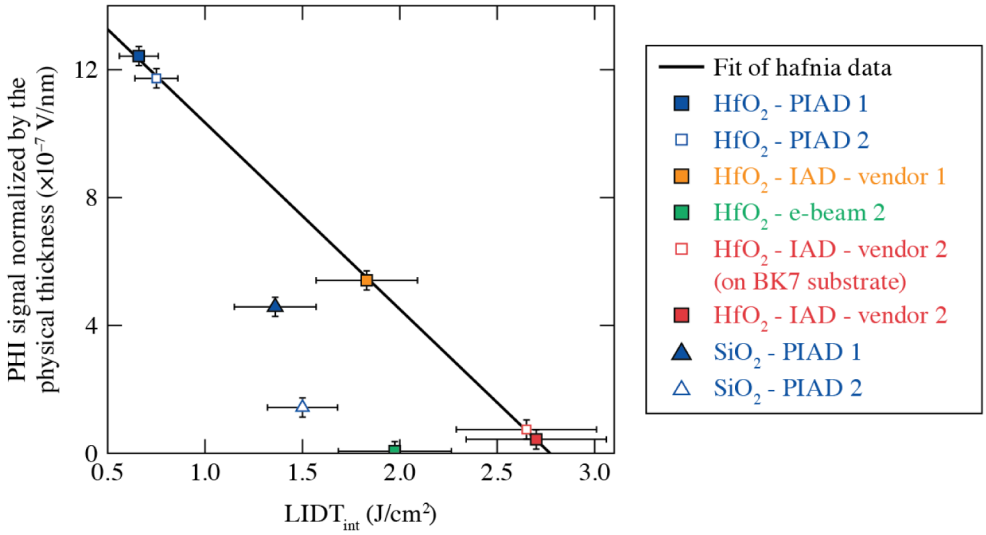

Fig. 5. Photothermal heterodyne imaging (PHI) signal at 355 nm normalized by the physical thickness as a function of the intrinsic LIDT for hafnia (squares) and silica (triangles) samples.

4. Conclusions

In this work we investigated the role of the deposition method for both silica and hafnia layers and their corresponding absorption edge spectral characteristics on the LIDT of the as-fabricated materials ($LIDT_{int}$). For that purpose, we followed the same characterization methods on different samples fabricated through three different deposition techniques, namely plasma ion-assisted deposition (PIAD), electron-beam evaporation, and ion-assisted electron-beam evaporation by two different vendors (IAD vendor 1 and IAD vendor 2). This study explores nondestructive methods to predict the intrinsic LIDT of materials. They are based on the assumption that damage results from the formation of a near-solid-state conduction-band electron population that is enabled by multiphoton absorption, excited via intraband transitions or transitions assisted by defect and localized states in the band gap. These states enhance the electron-transition probability to the conduction band, thereby decreasing the laser fluence/intensity associated with the laser-damage threshold. By combining ellipsometry measurements, numerical calculations of the field intensity enhancement, measurements of the LIDT, and optical gap determined by the Tauc method, we showed that even if the fabrication process (deposition method and vendor expertise) weakly influences the optical gap (Tauc) energy of the material, it strongly influences $LIDT_{int}$ of the two materials. This highlights the fact that the intrinsic LIDT of an oxide material cannot be predicted based solely on knowledge of the optical gap energy. A better correlation with the $LIDT_{int}$ was observed when considering the strength of the absorption below the optical gap. This was evaluated by directly measuring both the absorption spectra and the photothermal absorption. We show novel results that indicate a correlation between photothermal absorption in the UV and intrinsic LIDT in the near infrared. This approach may pave the way for the development of nondestructive methods of evaluating the LIDT of a

Optics EXPRESS

material and/or developing *in situ* material characterization approaches during the coating deposition.

Funding

Department of Energy National Nuclear Security Administration (DE-NA0003856); University of Rochester; New York State Energy Research and Development Authority.

Acknowledgment

We thank Christophe Licitra (*Commissariat à l'Énergie Atomique et aux Énergies Alternatives, LETI, Grenoble*) for the band-gap energy measurements.

References

1. J. D. Zuegel, S. Borneis, C. Barty, B. LeGarrec, C. Danson, N. Miyanaga, P. K. Rambo, C. LeBlanc, T. J. Kessler, A. W. Schmid, L. J. Waxer, J. H. Kelly, B. Kruschwitz, R. Jungquist, E. Moses, J. Britten, I. Jovanovic, J. Dawson, and N. Blanchot, "Laser challenges for fast ignition," Fus. Sci. Technol. **49**(3), 453–482 (2006).
2. M. Koga, Y. Arikawa, H. Azechi, Y. Fujimoto, S. Fujioka, H. Habara, Y. Hironaka, H. Homma, H. Hosoda, T. Jitsuno, T. Johzaki, J. Kawanaka, R. Kodama, K. Mima, N. Miyanaga, M. Murakami, H. Nagatomo, M. Nakai, Y. Nakata, H. Nakamura, H. Nishimura, T. Norimatsu, Y. Sakawa, N. Sarukura, K. Shigemori, H. Shiraga, T. Shimizu, H. Takabe, M. Tanabe, K. A. Tanaka, T. Tanimoto, T. Tsubakimoto, T. Watari, A. Sunahara, M. Isobe, A. Iwamoto, T. Mito, O. Motojima, T. Ozaki, H. Sakagami, T. Taguchi, Y. Nakao, H. Cai, M. Key, P. Norreys, and J. Pasley, "Present states and future prospect of fast ignition realization experiment (FIREX) with Gekko and LFEX lasers at ILE," Nucl. Instrum. Methods Phys. Res. A **653**(1), 84–88 (2011).
3. L. J. Waxer, D. N. Maywar, J. H. Kelly, T. J. Kessler, B. E. Kruschwitz, S. J. Loucks, R. L. McCrory, D. D. Meyerhofer, S. F. B. Morse, C. Stoeckl, and J. D. Zuegel, "High-energy petawatt capability for the OMEGA laser," Opt. Photonics News **16**(7), 30–36 (2005).
4. A. Casner, T. Caillaud, S. Darbon, A. Duval, I. Thfouin, J. P. Jadaud, J. P. LeBreton, C. Reverdin, B. Rosse, R. Rosch, N. Blanchot, B. Villette, R. Wrobel, and J. L. Miquel, "LMJ/PETAL Laser Facility: Overview and opportunities for laboratory astrophysics," High Energy Density Phys. **17**(Part A), 2–11 (2015).
5. N. Blanchot, G. Béhar, J. C. Chapuis, C. Chappuis, S. Chardavoine, J. F. Charrier, H. Coïc, C. Damiens-Dupont, J. Duthu, P. Garcia, J. P. Goossens, F. Granet, C. Grosset-Grange, P. Guerin, B. Hebrard, L. Hilsz, L. Lamaignere, T. Lacombe, E. Lavastre, T. Longhi, J. Luce, F. Macias, M. Mangeant, E. Mazataud, B. Minou, T. Morgaint, S. Noailles, J. Neauport, P. Patelli, E. Perrot-Minnot, C. Present, B. Remy, C. Rouyer, N. Santacreu, M. Sozet, D. Valla, and F. Laniesse, "1.15 PW-850 J compressed beam demonstration using the PETAL facility," Opt. Express **25**(15), 16957–16970 (2017).
6. A. A. Kozlov, J. C. Lambropoulos, J. B. Oliver, B. N. Hoffman, and S. G. Demos, "Mechanisms of picosecond laser-induced damage in common multilayer dielectric coatings," Sci. Rep. **9**(1), 607 (2019).
7. J. H. Apfel, "Optical coating design with reduced electric field intensity," Appl. Opt. **16**(7), 1880–1885 (1977).
8. J. H. Apfel, J. S. Matteucci, B. E. Newnam, and D. H. Gill, "The role of electric field strength in laser damage of dielectric multilayers," in *Proceedings of the 8th Annual Symposium on Optical Materials for High Power Lasers* (National Bureau of Standards, 1976), pp. 301–390.
9. M. Chorel, T. Lanternier, É. Lavastre, N. Bonod, B. Bousquet, and J. Néauport, "Robust optimization of the laser induced damage threshold of dielectric mirrors for high power lasers," Opt. Express **26**(9), 11764–11774 (2018).
10. M. Mero, J. Liu, W. Rudolph, D. Ristau, and K. Starke, "Scaling laws of femtosecond laser pulse induced breakdown in oxide films," Phys. Rev. B Condens. Matter Mater. Phys. **71**(11), 115109 (2005).
11. A. Hervy, L. Gallais, G. Chériaux, and D. Mouricaud, "Femtosecond laser-induced damage threshold of electron beam deposited dielectrics for 1-m class optics," Opt. Eng. **56**(1), 011001 (2016).
12. L. Gallais and M. Commandré, "Laser-induced damage thresholds of bulk and coating optical materials at 1030 nm, 500 fs," Appl. Opt. **53**(4), A186–A196 (2014).

Optics EXPRESS

13. F. Urbach, "The long-wavelength edge of photographic sensitivity and of the electronic absorption of solids," Phys. Rev. **92**(5), 1324 (1953).
14. B. Sadigh, P. Erhart, D. Åberg, A. Trave, E. Schwegler, and J. Bude, "First-principles calculations of the Urbach tail in the optical absorption spectra of silica glass," Phys. Rev. Lett. **106**(2), 027401 (2011).
15. S. Papernov, M. D. Brunsman, J. B. Oliver, B. N. Hoffman, A. A. Kozlov, S. G. Demos, A. Shvydky, F. H. M. Cavalcante, L. Yang, C. S. Menoni, B. Roshanzadeh, S. T. P. Boyd, L. A. Emmert, and W. Rudolph, "Optical properties of oxygen vacancies in HfO_2 thin films studied by absorption and luminescence spectroscopy," Opt. Express **26**(13), 17608–17623 (2018).
16. "Evaluation of measurement data—Guide to the expression of uncertainty in measurement," JCGM 100:2008 (GUM 1995 with minor corrections), 1st. ed. (2008), https://www.bipm.org/utils/common/documents/jcgm/JCGM_100_2008_E.pdf
17. "International vocabulary of metrology—Basic and general concepts and associated terms (VIM) " JCGM 200:2011 (2008 version with minor corrections), 3rd ed. (2012), https://www.bipm.org/utils/common/documents/jcgm/JCGM_200_2012.pdf.
18. A. V. Tikhonravov and M. K. Trubetskov, OptiLayer Thin Film Software, Optilayer Ltd., http://www.optilayer.com.
19. K. Ohta and H. Ishida, "Matrix formalism for calculation of electric field intensity of light in stratified multilayered films," Appl. Opt. **29**(13), 1952–1959 (1990).
20. M. Sozet, J. Néauport, E. Lavastre, N. Roquin, L. Gallais, and L. Lamaignère, "Laser damage density measurement of optical components in the sub-picosecond regime," Opt. Lett. **40**(9), 2091–2094 (2015).
21. B. Mangote, L. Gallais, M. Commandré, M. Mende, L. Jensen, H. Ehlers, M. Jupé, D. Ristau, A. Melninkaitis, J. Mirauskas, V. Sirutkaitis, S. Kičas, T. Tolenis, and R. Drazdys, "Femtosecond laser damage resistance of oxide and mixture oxide optical coatings," Opt. Lett. **37**(9), 1478–1480 (2012).
22. J. Tauc, R. Grigorovici, and A. Vancu, "Optical properties and electronic structure of amorphous germanium," Phys. Status Solidi, B Basic Res. **15**(2), 627–637 (1966).
23. B. C. Stuart, M. D. Feit, A. M. Rubenchik, B. W. Shore, and M. D. Perry, "Laser-induced damage in dielectrics with nanosecond to subpicosecond pulses," Phys. Rev. Lett. **74**(12), 2248–2251 (1995).
24. L. A. Emmert, M. Mero, and W. Rudolph, "Modeling the effect of native and laser-induced states on the dielectric breakdown of wide band gap optical materials by multiple subpicosecond laser pulses," J. Appl. Phys. **108**(4), 043523 (2010).
25. B. C. Stuart, M. D. Feit, S. Herman, A. M. Rubenchik, B. W. Shore, and M. D. Perry, "Nanosecond-to-femtosecond laser-induced breakdown in dielectrics," Phys. Rev. B Condens. Matter **53**(4), 1749–1761 (1996).
26. S. Papernov, A. Tait, W. Bittle, A. W. Schmid, J. B. Oliver, and P. Kupinski, "Near-ultraviolet absorption and nanosecond-pulse-laser damage in HfO_2 monolayers studied by submicrometer-resolution photothermal heterodyne imaging and atomic force microscopy," J. Appl. Phys. **109**(11), 113106 (2011).